

THE SEARCH FOR DARK MATTER
WITH XENON1T

A Dissertation
Submitted to the Faculty
of
Purdue University
by
Darryl Masson

In Partial Fulfillment of the
Requirements for the Degree
of
Doctor of Philosophy

May 2018
Purdue University
West Lafayette, Indiana

TABLE OF CONTENTS

	Page
LIST OF TABLES	iv
LIST OF FIGURES	v
SYMBOLS	vii
ABBREVIATIONS	viii
ABSTRACT	ix
1 The Case for Dark Matter	1
1.1 Astrophysical Evidence for Dark Matter	1
1.1.1 Rotation curves	1
1.1.2 Gravitational Lensing	3
1.1.3 Galaxy cluster dynamics	4
1.2 Cosmological Evidence for Dark Matter	7
1.2.1 Big Bang Nucleosynthesis (BBN)	7
1.2.2 Cosmic Microwave Background (CMB)	8
1.2.3 Baryoacoustic Oscillations (BAO)	8
1.2.4 Structure Formation	8
1.3 Dark Matter in the universe today	8
1.3.1 Weakly Interacting Massive Particles (WIMPs)	9
1.3.2 Massive Compact Halo Objects (MACHOs)	9
1.3.3 Axions	10
1.3.4 Neutrinos	10
2 The Search for Dark Matter	11
2.1 Production Searches	11
2.2 Annihilation Searches	12
2.3 Scattering Searches	12
2.3.1 Searching with Germanium	12
2.3.2 Searching with Liquid Nobles	13
3 The XENON1T Experiment	15
3.1 Operational Overview	15
3.2 System Overview	16
3.2.1 Water Cherenkov Muon Veto	16
3.2.2 Belt systems	16
3.2.3 Gas recirculation and purification	17

	Page
3.2.4 Electronics and DAQ	17
3.2.5 TPC	17
4 Nuclear Recoil (NR) Calibrations	19
4.1 Flux calibrations	20
4.2 Pulse Shape Discrimination (PSD)	20
4.2.1 Charge Comparison Method (CCM)	21
4.2.2 Fourier Series Analysis (DFT)	21
4.2.3 Laplace Transformations (LT)	21
4.2.4 Fitting with Standard Events	21
5 Electronic Recoil (ER) Calibrations	25
5.1 Introduction	25
5.2 γ -Measurements of Filter Deposition	29
5.3 ^{222}Rn Emanation Measurement	33
5.4 Si PIN Diode Measurements	33
5.5 γ -Spectroscopy of Pipe Contamination	36
5.6 Measurements of Filter Efficacy	37
5.7 Mixing in a Liquid Xenon Detector	41
5.8 Interpretation	45
5.9 Conclusions	46
VITA	47

LIST OF TABLES

Table	Page
4.1 Cuts used to select events to average to create standard events	22
5.1 The decay chain of primordial thorium, sometimes called the 4n series .	26
5.2 Measurements of radionuclide release from the ^{220}Rn source collected in filter paper.	30
5.3 Results of the measured γ -activity in the cold-welded copper pipe after flushing argon through source and pipe.	36
5.4 Calculated values and limits on ^{224}Ra and ^{228}Th release from deposition in the copper pipe after argon flushing.	37
5.5 Measurement results for the 0.5 micron sintered and ceramic filters . .	39
5.6 Summary of all measurements of emanation rates, given in units of atoms/min/kBq.	44

LIST OF FIGURES

Figure	Page
1.1 Rotation curve of M33, from [?]	3
1.2 The Bullet Cluster of galaxies, from [?]	6
3.1 An idealized event inside a dual-phase TPC	16
5.1 A simulation of the β -spectrum of ^{212}Pb . The feature at 240 keV is due to decay modes with an associated γ that adds to the energy observed in the decay.	28
5.2 ^{228}Th is deposited onto a 30 mm stainless steel disc (left). It is held in a simple emanation vessel (right) for mounting on a noble gas system. . .	29
5.3 Gamma spectrum taken of the filter 7.2 days after exposure showing the ^{212}Pb line at 238.6 keV and the ^{224}Ra line at 241.0 keV. The dashed and solid lines are from a fit to the data.	32
5.4 Total activity in the Si PIN diode above 1 MeV. The data points include statistical error bars, barely visible on this scale. The line is the fit of an exponential plus constant baseline.	35
5.5 Activity of $^{212}\text{BiPo}$ in the Si PIN diode during and after flushing xenon through the ceramic filter. An exponential was fitted to the decaying part, yielding a half-life of (10.64 ± 0.05) h in excellent agreement with the ^{212}Pb half-life of (10.64 ± 0.01) h [?].	38
5.6 Decay to background of $^{212}\text{BiPo}$ in the Si PIN diode for the measurement of the sintered filter. An exponential and a constant are fitted to the data. The band is the previously measured background of the detector. . . .	39
5.7 Energy spectrum taken with the Si PIN diode from two sintered filters that were placed in series directly after the source in a xenon gas recirculation system.	40
5.8 Schematic of the recirculation loop for the liquid xenon detector measurement. The liquid is evaporated in the heat exchanger and is pumped through the purifier, where it can then be flushed past the ^{220}Rn source or injected directly back to the detector.	42

5.9	Trigger rate in the liquid xenon detector before, during, and after source exposure. The spike in the rate after opening the source clearly shows the introduction of activity into the target volume, and the decay after it the source was closed indicates the presence of ^{212}Pb	43
-----	---	----

SYMBOLS

m mass

v velocity

ABBREVIATIONS

LXe	Liquid xenon
GXe	Gaseous xenon
TPC	Time projection chamber
WIMP	Weakly interacting massive particle
DM	Dark matter

ABSTRACT

Masson, Darryl PhD, Purdue University, May 2018. The Search for Dark Matter with XENON1T. Major Professor: Rafael Lang.

This is where the abstract goes. Not much to say yet.

1. The Case for Dark Matter

For most of the last century evidence for the existence of dark matter has been gathering from various sources. Initially, evidence was primarily from astrophysical observations of the behaviour of various structures observed in the universe. However, once cosmology became a predictive tool, more stringent requirements could be placed on the unseen parts of the universe. We will begin by evaluating the astrophysical and cosmological evidences for the existence of dark matter, and discussing some proposed models.

1.1 Astrophysical Evidence for Dark Matter

The first indications that something was amiss in astronomy was from observations made of what was then the Andromeda Nebula by Heber Curtis in 1917 [1]. Based on these observations, Curtis concluded that the Nebula was actually an entirely separate galaxy at some immense distance from the Milky Way. In the 1920s Edwin Hubble showed conclusively that the universe was much more than just our Milky Way galaxy [2]. The next logical step was for astronomers to study this recently-discovered rest of the universe. Very soon it became clear that there was a great deal about which we knew very little.

1.1.1 Rotation curves

In the early 17th century Johannes Kepler published his three laws of planetary motion [3]. Kepler's Third law states gives us a relationship between an orbit's

period, semimajor axis (radius, if circular), and enclosed mass. Assuming the mass distribution is a function purely of radius, we can define

$$M(r) = \int_0^r d^3r' \rho(r') = 4\pi \int_0^r dr' r'^2 \rho(r') \quad (1.1)$$

We can do a bit of manipulation on the expression Kepler found to give us a relationship relating the expected orbital velocity of an object in a galaxy as a function of its distance from the galactic core,

$$v(r) = \sqrt{\frac{GM(r)}{r}} \quad (1.2)$$

Armed with (??) and (1.2), we can calculate $M(r)$ by observing a galaxy with telescopes and assuming some stellar mass distribution, and then make some prediction for $v(r)$. Using Doppler-shifted lines of stars or dwarf galaxies, the orbital velocities can be measured and compared to the prediction from the mass distribution. The predicted and measured rotation speeds bear only marginal resemblances to each other, as seen in figure 1.1, an image of the Triangulum galaxy (M33).

Clearly, something is wrong with the predictions. If we assume that stars, gas, dust, and other objects visible with telescopes are all there is to a galaxy, then at large distances from the galactic center it will increasingly appear like a point mass, giving the familiar relationship $v(r) \propto r^{-3/2}$ that is Kepler's third law. In the bulge in the center of the galaxy, we see the speed increases roughly linearly with the radius, indicating a mass distribution proportional to r^3 , or a constant density profile. However, the data clearly shows that at large r , the velocity is approximately constant, indicating a mass distribution proportional to r or a density profile proportional to $1/r^2$. If there is something in the galaxy that would produce this distribution of mass it doesn't show up in any telescope. Additionally, the stars near the edge of the galaxy are well above the predicted escape velocity $v_{\text{esc}} = \sqrt{2}v_{\text{circ}}$, and as galaxies are stable over astronomical periods of time, they cannot be filled with objects exceeding the escape velocity.

This data indicate one of two things. Either Kepler's Law and the Newtonian gravity upon which it is based are invalid on galactic distance scales, or there is some

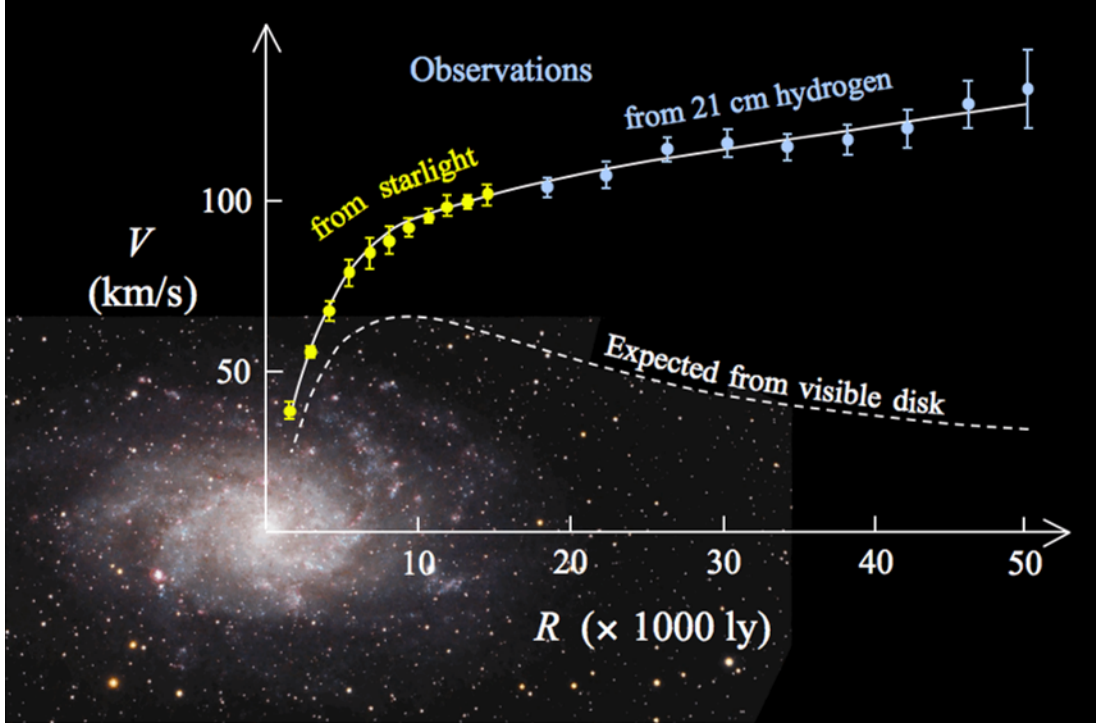


Figure 1.1. Rotation curve of M33, from [?]

hidden mass or dark matter filling a galaxy. Supposing the first case to be true, the recourse would be to introduce modifications to gravity that only act over long distances, which has been done with some limited success [?, ?, ?]. In the second case, some distribution of mass must be inferred that has a negligible contribution in the inner parts of the galaxy but becomes dominant as one goes further out. A number of distributions have been proposed [?, ?] which will address the rotation curve problem.

1.1.2 Gravitational Lensing

One prediction of Einstein's Theory of General Relativity is that any concentration of matter and energy will act as a lens for passing photons by distorting spacetime []. When lensing is observed, forward modelling can be performed to estimate the distribution and amount of matter present.

Strong lensing

Provided the alignment of the stars is correctly and the foreground lensing object is sufficiently massive, the image of a distant object can be lensed strongly around the foreground object, resulting in multiple images or severe distortions. Strong lensing tends to be easy to identify (for instance, most galaxies when viewed edge-on don't bear strong resemblances to a banana). In all cases, the observed distortions require much more mass than can be observed with telescopes.

Weak lensing

In cases where the lensing object is not sufficiently dense or massive to create obvious strong lensing, weak lensing can still be observed. Weak lensing can be measured using statistical methods by creating an average shape of a galaxy in the field of view and calculating some distortion parameter. A distribution of distortion can be created, which will indicate where the greatest concentrations of mass are.

1.1.3 Galaxy cluster dynamics

The observations of the dynamics of clusters of galaxies yields fairly clear indication that dark matter must form a significant contribution to the mass of a galaxy cluster. When observations are made of clusters other than our own Local Group, a good deal of hot gas is observed. This hot gas radiates x-rays (and thus is often called hot x-ray gas), and from its luminosity both the temperature and mass can be measured. The extremely high temperatures observed are from basic energy conservation. As the gas falls into the cluster's gravitational potential well, it gains kinetic energy, which, for a gas, is equivalent to temperature. The temperature of the gas thus gives an indication of the depth of the potential well. Applying the Virial theorem ($2K + U = 0$) to the cluster, the kinetic energies of the component galaxies can be measured and compared to the observed potential energy. In both cases, the required potential

well is much deeper than could be formed from merely the hot gas and the galaxies themselves, despite the fact that there is an order of magnitude more mass in gas than in galaxies. Indeed, the extra mass required to make the system behave is an order of magnitude greater than the mass that is observed.

Bullet Cluster

The Bullet Cluster (1E 0657-558) is an excellent example of both galaxy cluster dynamics and weak lensing, and also furnishes additional information on dark matter. Figure 1.2 is a composite image of a Hubble Space Telescope (HST) image and a Chandra X-ray Observatory image. The pink is the hot x-ray gas (seen by Chandra), and forms the majority of the baryonic mass of the cluster. The powerful shock produced during the collision is clearly seen in the subcluster on the right, giving indications of the speed of the collision, and also the mass of that subcluster.

A good deal of information can be gleaned from a careful inspection of figure 1.2. The first thing to note is the separation of two populations of baryonic matter. In the visible wavelengths we observe the two subclusters with their galaxies largely undisturbed by their transit. The distance between galaxies in a cluster is larger than the characteristic size of a galaxy, thus a cluster is dominated by the star-less space between galaxies. When two galaxy clusters collide the chance of a direct collision between two galaxies is small, as the gaps for galaxies to slot between each other are larger than the galaxies themselves. Thus, we see that the two subclusters have been largely unaffected by their passage.

However, a respectable galaxy cluster contains far more than just galaxies. The majority of the mass comes from free hydrogen in the form of the hot x-ray gas. When two populations of gas pass through each other, they interact differently from galaxies. While the distance between atoms in a low-density gas is much larger than the size of the atoms and the mean free path is very long, this gas radiates x-rays which means the atoms are moving very quickly. The gas interacts significantly as



Figure 1.2. The Bullet Cluster of galaxies, from [?]

the two clouds pass through each other, which slows the gas down. Thus, as the two subclusters move away from each other post-collision, the x-ray gas will have lost some kinetic energy due to its interactions and will not leave the collision center as quickly as the stars and galaxies. This leads to a separation of the galaxies from the gas.

However, if a weak lensing study is performed on this cluster, it indicates that the lensing centers, and thus the greatest concentrations of mass, are centered around the galaxies, not the gas. This at first presents a dilemma, as the luminosities observed require that there be much more mass in gas than in galaxies. How, then, could the

lensing be centered around somewhere the mass isn't? The answer is that there must be some hidden mass that accompanies each subcluster. Furthermore, we can note that this hidden mass didn't separate out with the gas, indicating that it doesn't experience significant self-interactions.

1.2 Cosmological Evidence for Dark Matter

While astrophysics tends to provide the prettier pictures, cosmology imposes more stringent numerical limits on dark matter and its distributions.

1.2.1 Big Bang Nucleosynthesis (BBN)

About a minute after the Big Bang, the universe had cooled sufficiently to allow nuclei to form and not be immediately broken apart due to the high ambient temperature. A good deal had happened in this minute, including the annihilation of all the antimatter with almost all the matter, creating the ocean of photons that is now the cosmic microwave background. It will prove convenient to define η as the ratio between the number of baryons and the number of photons, or, as the number of photons is large, $\eta_{10} = 10^{10}\eta$. Neutrons and protons had just fallen out of numerical equilibrium due to their small difference in mass, and now existed in a ratio of about 1 neutron per 7 protons. Neutrons and protons first combined to make deuterium, then as the deuterium abundance increased, deuterium fused with deuterium to produce tritium and then with tritium to produce ^4He . This epoch continued for just under half an hour, until expansion had driven particles far enough apart that collisions became infrequent and the temperature had decreased below the energy necessary to overcome the Coulomb repulsion between nuclei. Now, nearly all of the universe's neutrons were in helium due to its stability. Of the remaining few neutrons, most were in deuterium, with a few in ^7Li . Due to its stability, the population of ^4He depends very little on η_{10} , but deuterium is not strongly bound, so a smaller η_{10} (more photons) means fewer deuterium nuclei. By measuring the primordial abundance of

deuterium, this will admit a value of η_{10} which will in turn indicate what percentage of the universe was baryons at this epoch.

1.2.2 Cosmic Microwave Background (CMB)

Pensias and Wilson were the first to turn a sensitive microwave telescope to the skies [?,?], and their discovery earned them the Nobel Prize in Physics in 1978. Now, the best measurements of the CMB come from satellites like WMAP and Planck. The basic data taken are nearly totally featureless and isotropic to a few parts per million as shown in Fig. ??a. If the average temperature of 2.7K is subtracted, a dipole term appears arising from the Sun's movement around the galaxy (Fig. ??b). In a sense, this indicates a favored reference frame for our universe, that is, one in which the observer is at rest relative to the CMB. If this dipole term is subtracted, the galactic contributions become clear (Fig. ??c). Subtracting this yields a density map of the universe when the CMB decoupled from the baryonic matter (about 380,000y after the Big Bang, Fig. ??d). Certain regions contain a slightly higher density than others, indicating a greater concentration of stuff. This temperature map can be expanded in the spherical harmonics and a power spectrum plotted. A cosmological model is then fitted to this spectrum, and from this model various parameters of our universe can be extracted.

1.2.3 Baryoacoustic Oscillations (BAO)

1.2.4 Structure Formation

1.3 Dark Matter in the universe today

The burning question now is, what might dark matter be? The stuff must exist, so testable models should be proposed.

1.3.1 Weakly Interacting Massive Particles (WIMPs)

Observations (or lack thereof) of dark matter exclude interactions via electromagnetism and the strong force. However, this does not exclude weak interactions.

Freezeout and the WIMP Miracle

Supposing a population of particles existed in equilibrium with the rest of the universe at some early epoch (before BBN), as the universe expanded and cooled the production and annihilation reactions would begin to fall out of equilibrium. At some point, the universe was hot enough to allow for $\chi\bar{\chi} \leftrightarrow f\bar{f}$. However, once the temperature had dropped, the reverse reaction would become impossible, leaving $\chi\bar{\chi} \rightarrow f\bar{f}$. Eventually even this would become impossible, leaving no allowed reactions.

1.3.2 Massive Compact Halo Objects (MACHOs)

The limits on non-baryonic matter deriving from the CMB rely on the lack of detectable interaction with the CMB. However, there are more things that interact with the CMB in ways that our telescopes aren't sensitive enough to detect. The MACHO theory posits a dark matter halo filled with massive compact baryonic objects such as unowned Jupiter-sized planets, dwarfs, and small, quiet black holes. Such objects would radiate only very weakly, which would be very difficult for telescopes to directly identify. Detection of these objects is principally done through observation of micro-lensing events, where a MACHO passes in front of a background star in such a way that the gravitational lensing acts to greatly magnify the star. Modelling is then done to identify both the location and mass of the lensing object. These events have been observed but the frequency with which they happen only admits $\sim 1\%$ of the required mass of dark matter \square .

1.3.3 Axions

Originally proposed as a solution to the strong-CP problem, axions were suggested to be dark matter candidates in [1].

1.3.4 Neutrinos

The elephant in the room at this point is neutrinos. Neutrinos only interact via the weak and gravitational forces, and should be dead ringers for dark matter. Why, then, are we still looking? The answer lies in temperature. Due to the extremely low mass of neutrinos, any amount of energy greater than a few eV is sufficient to make the neutrino ultrarelativistic. Additionally, there are no mechanisms whereby a lot of neutrinos can lose a lot of energy. So, once a neutrino is created, it will tend to hold on to whatever energy it has.

Now, if the early universe was filled with ultrarelativistic matter, the structure formation we observe today could not have occurred. Any overdensity of ultrarelativistic matter will have a greater outflux than influx, which will tend to smoothe out any tendency of matter to clump under the influence of gravity. During the period of primary structure formation, most of the universe's neutrinos would have been ultrarelativistic, and so if they had been a significant component of dark matter the universe today would have a much more uniform distribution of mass, as opposed to the observed scattered delta functions. Additionally, Planck limits Ω_ν to $< \text{value [2]}$, which is far too low to be a dominant component.

2. The Search for Dark Matter

Now that a promising model of dark matter have been proposed, some time should be spent discussing how it might be tested. There are three classes of experiments to detect WIMPs. One can try to produce them by smashing known standard model particles together. Or, one can try to observe two WIMPs smashing into each other and annihilating. Thirdly, one can try to observe a WIMP directly interacting with some standard model particle. We will discuss these three methods, their limitations, and their strengths.

2.1 Production Searches

Were one to take two standard model particles, give them together with gratuitous amounts of energy, and and smash them into one another, one generally produces a large menagerie of other particles that tend to decay fairly quickly. However, assuming there is some nonzero coupling between dark matter and the standard model, there is a probability that instead of producing other standard model particles, the collision will produce dark matter which will leave the detector without causing it to trigger. The signature of this will be missing energy and momentum from the collision. The goal, then, is to search through reams of data for these signatures. However, if there isn't a trigger there is no evidence that anything happened in the detector. This means one has to look for cases where both dark matter and standard model particles are created (so something can cause a trigger), but each additional coupling in the Feynman diagram is accompanied by a reduced probability. As the strength of these couplings is not known, this process is a little like searching for a needle in a haystack when you don't know what a needle looks like.

2.2 Annihilation Searches

Given the density of dark matter observed today, there is some finite probability that two dark matter particles will run into each other with sufficient energy to annihilate. If we happen to be fortunate enough to be pointing a telescope towards this event at the appropriate time, its signature could be detected. The goal here is to filter out which events are from known astrophysical sources and which are the dark matter signals. This is never straightforward. One could compare it to searching for a needle in a stack of slightly different needles. On numerous occasions, peaks have shown up in the data to some significance, but then vanish once a complementary experiment begins collecting data in that region of the spectrum. Additionally, the astrophysical sources are not yet completely understood.

2.3 Scattering Searches

We can continue to rotate our Feynman graph to demonstrate a scattering event. In a scattering event, the interaction between the dark matter particle and the target standard model particle will cause the target to recoil. The information generated in this event will be contained in the ionization of the target atom, its resulting scintillation, and the creation of phonons as the nucleus recoils into its neighboring atoms. Depending on the specifics of the detector, some combination of these can be collected. The two leading technologies in this field are based on germanium crystals and liquid noble time projection chambers (TPCs).

2.3.1 Searching with Germanium

The leading group searching for WIMPs with germanium detectors is the CDMS collaboration [1]. Germanium detectors are capable of collecting the scintillation and phonons created during a WIMP scattering event.

Advantages of Using Germanium

Semiconductors have been studied for many decades and by now are very well understood. Therefore, detectors based on this technology have the advantage of a mature field of research into the systematic effects of these devices. There are a great many facilities around the world that deal with semiconducting devices. Additionally, the germanium yields excellent sensitivity to lower-mass WIMPs ($< 10 \text{ GeV}/c^2$).

Disadvantages of Using Germanium

The most significant disadvantage of the use of germanium crystals is the practical limits to the size of crystal that can be grown. To maximize exposure, experiments generally wish for the greatest target mass possible. With germanium, this can only be accomplished by creating a large array of individual crystals. As the array will not form one large crystal structure, each component crystal and its attached detection apparatus are subject to surface effects like radon or trace radioactivity in the hardware.

2.3.2 Searching with Liquid Nobles

This class of detector includes all TPCs filled with some noble elements. Xenon is the most popular element used, but argon is also used. The two main players using xenon-based TPCs are the LUX and XENON collaborations [1]. The LUX detector is based in the Sanford Underground Research Facility in South Dakota, USA, while XENON is based at Laboratori Nazionali del Gran Sasso (LNGS) in central Italy. These detector types are designed to collect the scintillation and ionization created in a WIMP scattering event through the combination of a bulk liquid target and a small gas layer above it.

Advantages of Liquid Nobles

A clear advantage of the use of the TPC is the ability to scale. While calibrations for very large detectors become more challenging, it is much simpler to build a TPC with 1000kg target mass than to grow a 1000kg germanium crystal. Thus, argon- and xenon-based detectors will continue to dominate in terms of exposure. Also, the mass of xenon lends itself well to great sensitivity with higher-mass WIMPS ($> 10 \text{ GeV}/c^2$). As this mass range is heavily favored by supersymmetric WIMP models, these detectors are poised to probe this promising region of the parameter space.

3. The XENON1T Experiment

The leading WIMP direct detection experiment is run by the XENON collaboration, of which XENON1T is the latest version of a series of ever-larger detectors [1]. Built in central Italy at Laboratori Nazionali del Gran Sasso (LNGS), XENON1T is the largest and most sensitive xenon dual-phase time projection chamber (TPC) in the world at the time of commissioning, containing 3300 kg of xenon.

3.1 Operational Overview

The operation of a dual-phase TPC is as follows. When something interacts with an atom (xenon, argon, etc) inside the detector, it will free a number of electrons, either directly or via the deexcitation of the nucleus after scattering inelastically. Some of these electrons will recombine instantly with the ion, producing scintillation light that is collected with the top and bottom PMT arrays. This signal is variably called the S1, prompt, or scintillation signal. An electric field is applied to the target volume, so some of the electrons will drift upwards towards the surface of the liquid. The ion would drift down and eventually collect electrons from the cathode mesh near the bottom of the detector, but convection currents inside the detector [?] dominate over the ion drift speed. Once the electrons reach the surface of the liquid, they will enter the gas and accelerate very quickly in the lower-density xenon gas. These energetic electrons will interact with the gas, creating more light that is again collected. This signal is variably called the S2, delayed, or ionization signal. The time difference between the S1 and S2 is the amount of time the electrons were drifting, and yields the depth or z coordinate of the interaction. The hit pattern on the top PMT array yields the (x,y) position of the event, as the PMTs directly above the

drifting electrons will see more photons and produce a stronger signal. Figure 3.1 shows schematically a typical event.

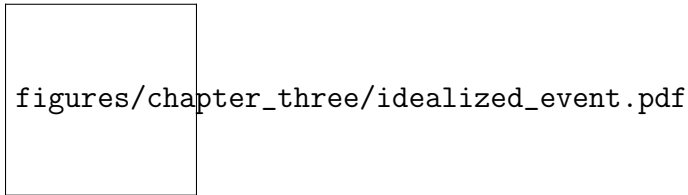


Figure 3.1. An idealized event inside a dual-phase TPC

3.2 System Overview

The XENON1T detector is composed of numerous subsystems, which will be discussed here in some detail.

3.2.1 Water Cherenkov Muon Veto

The detector is housed in the center of a large tank of high-purity water, 10m in diameter and 10m in height. While the rock overburden at LNGS reduces the cosmogenic muon flux by many orders of magnitude [1], these muons typically have extremely high energies and take a long time to fully dissipate all their energy. Thus, muons can still regularly traverse the detector volume. However, by surrounding the detector with water, the muons will create Cherenkov radiation. An array of PMTs placed in the water can detect the light and a coincident event in the detector itself tagged.

3.2.2 Belt systems

Three systems of belts are mounted in the water tank around the detector to facilitate positioning radioactive sources around the TPC to perform various tasks like electron livetime calibrations and self-shielding measurements. Two of these

systems have purely vertical travel (I-belts), and the third is capable of moving a source all the way underneath the detector along a secant (U-belt).

3.2.3 Gas recirculation and purification

A large series of tubes exists to support the operation of the detector. The primary purpose of this system is to fill the detector at the beginning of a run, to introduce radioactive sources into the detector for various calibrations, to maintain the purity of the xenon in the detector by recirculating through a getter during the run, and to recover the xenon at the end of a run.

3.2.4 Electronics and DAQ

3.2.5 TPC

The TPC itself is housed inside the inner cryostat and is made of only the most radiopure materials available.

4. Nuclear Recoil (NR) Calibrations

In XENON100 nuclear recoil calibrations were done through use of YBe and AmBe [?]. However, the several meters of water surrounding the outer cryostat are very good at moderating and absorbing neutrons. While there's no reason why a source cannot be lowered into the water tank next to the detector or a beam pipe installed and moved into position for use [?], there is a better way. YBe and AmBe both produce a spectrum of neutron energies. Also, XENON1T is big enough that it will be possible to resolve multiple scatters within the fiducial volume. This allows the possibility of using multiple scatters to perform the energy calibration. Recall elastic scattering between two objects. Given the scattering angle of the target, we can find the energy deposited using

$$E_{recoil} = \frac{2E_n}{\frac{m_n}{m_{Xe}}(1 + \frac{m_{Xe}}{m_n})^2}(1 - \cos \theta) \quad (4.1)$$

Here, E_n is the energy in the incident neutron, m_{Xe} and m_n are the masses of the xenon and the neutron, and θ is the scattering angle. If the neutrons are monoenergetic, then a very precise nuclear recoil calibration can be performed in situ by selecting various scattering angles. Monoenergetic neutrons can easily be created from fusion reactions, of which two candidates are ${}^2_1D + {}^2_1D \rightarrow {}^3_2He(0.82\text{MeV}) + n(2.45\text{MeV})$ (50% branching ratio) and ${}^2_1D + {}^3_1T \rightarrow {}^4_2He(3.6\text{MeV}) + n(14.1\text{MeV})$.

A DD reaction neutron generator was acquired from NSD Fusion for the purpose of performing the nuclear recoil calibrations on XENON1T. Detectors selected to calibrate it are liquid scintillators containing the chemical EJ-301, an organic liquid polymer with high hydrogen density, manufactured by Eljen Technologies, which is identical to the older and more well-known NE-213.

4.1 Flux calibrations

The neutron generator employs inertial electrostatic confinement (IEC) to achieve fusion. In IEC fusors, a cage in the middle of the chamber is held at some high voltage. Deuterium gas is injected into the (otherwise evacuated) chamber and ionized, which causes the deuterons to fall inwards towards and then into the cage. When a sufficient population of ions has been achieved, they form a virtual anode just inside the actual cage mesh. This provides sufficient extra electric field strength to contain the deuterons and enough energy for some to achieve fusion. Half of the fusion reactions will produce the desired monoenergetic neutron, the other branching ratio is ${}^2_1D + {}^2_1D \rightarrow {}^3_1T(1.01\text{MeV}) + p^+(3.02\text{MeV})$. Now, the reaction rate depends on the high voltage and current applied to the confining cage. To understand the operation of the neutron generator, the response to these parameters must be understood.

4.2 Pulse Shape Discrimination (PSD)

EJ-301 is sensitive to both fast neutrons and γ particles, but reacts differently to them. Neutron signals appear differently from γ signals because the γ only excites the electrons into a short-lived singlet state, where the neutron promotes the electrons into a longer-lived triplet state [1]. Processing algorithms can be written to discriminate between waveforms of these two particles. The work-horse algorithm, used since the ancient times of analog processing, is known as the Charge Comparison Method [2]. The advent of digital computing and cheap data storage means that data processing now does not necessarily need to be done live, allowing many other algorithms to be used for discrimination.

Traditionally, the quantification of discrimination was done by making a histogram of the discrimination parameter, fitting Gaussian curves to the neutron and γ populations, and defining a Figure of Merit as the separation of the peaks divided by the sum of the full widths at half maximum. However, the two populations in question

are not generally Gaussians, so this is like trying to measure a round hole with a square peg.

4.2.1 Charge Comparison Method (CCM)

This is a method based on two integration windows or gates of the pulse. One window is called the fast or short window, the other the slow or long window. The discrimination parameter used to differentiate these two types of pulse is the ratio of the slow integral value to the fast integral value. If the end of the fast window coincides approximately with the end of the typical γ pulse, the slow window will contain very little other than the baseline, so the discrimination parameter will be close to unity. For neutron events, however, the pulse contains a significant tail that extends beyond the end of the fast window, which is captured by the slow window. In this case, the discrimination parameter will be somewhat above unity.

4.2.2 Fourier Series Analysis (DFT)

4.2.3 Laplace Transformations (LT)

4.2.4 Fitting with Standard Events

Once some discrimination has been done with a reasonably reliable method, it is possible to create a standard waveform of each of the neutron and γ events. Events that pass a discrimination cut can be selected, aligned, and averaged. This will create a standard event or template waveform characterizing a detector's response to a given particle type. The advantage of this is that it will tend to reduce the effects of electronic noise. These standard events can then be fit to a captured waveform. Free parameters of the fit are a vertical offset or baseline shift, a horizontal offset or trigger shift, and a vertical scaling parameter. If the waveforms used to generate the standard events are all of a very energy band, like the ^{137}Cs Compton edge (447

Cut	Events left	Acceptance
None	211528247	1.0
Energy	162881	7.7×10^{-4}
Pre-pulse RMS	162519	
Post-pulse RMS		
Neutron		
γ		

Table 4.1
Cuts used to select events to average to create standard events

keV), the fit will serve not only to discriminate between neutron and gamma events, but will also yield an accurate measurement of the energy of the event.

Generating Standard Events

To generate these standard events, one must first identify waveforms to use. This must be done via some other method of discrimination. The standard events should be made by averaging a set of events with an extremely high purity, so aggressive cuts should be made to this end. To ensure sufficient statistics, a combination of several dozen files of data collected with the NG were used. The cuts applied to these events are a cut in energy (to select events at the ^{137}Cs Compton edge), cuts in the CCM discrimination parameter (to select either neutron or γ events, cuts in the cleanliness of the waveforms (RMS values of the pre- and post-pulse baselines), and a cut in the location of the peak. The details of these cuts are given in table 4.2.4.

Next, the waveforms must all be aligned with some sample, such as the sample that triggered the event. Then, waveforms are averaged together to create a preliminary standard event. This preliminary standard event is then fit to all the waveforms that made it. Outliers to the distribution can then be identified and removed from the list

of suitable events. This process can be iterated several times to improve the quality of the standard events, but the gains rapidly diminish.

5. Electronic Recoil (ER) Calibrations

Liquid xenon is particularly good at absorbing β and γ radiation, so the methods used in XENON100 of placing sources on the exterior of the detector simply are no longer feasible for XENON1T due to the 7 cm of xenon between the TPC and inner cryostat. The solution, then, is to introduce some radioactive source into the detector itself and perform calibrations from the inside.

However, one must very carefully select the isotopes used. Obviously, the decay chain must contain some radiation useful for calibration. The isotope selected must be able to be mixed into the detector, but as importantly, you must be able to get it out again. Removing stuff from the detector can either be accomplished by recirculation or by letting the isotope decay.

An excellent candidate for the internal ER calibrations is ^{212}Pb . This isotope occurs in the decay chain of ^{220}Rn , which is also a noble element and therefore can easily be mixed into the xenon. ^{212}Pb decays to the ground state of ^{212}Bi with a branching ratio of 11.9% and a Q-value of 570 keV, which means a reasonable percentage of β particles will be in the required low energies. Finally, there is nothing long-lived in the rest of the decay sequence, which ends with ^{208}Pb .

5.1 Introduction

Various low-background experiments are searching for rare events such as neutrinoless double-beta decay [?] or dark matter scatters [?]. Time projection chambers (TPCs) using liquid noble elements such as argon and xenon are at the forefront of these investigations [?, ?, ?, ?, ?, ?]. As these detectors become large, new challenges arise in accurately calibrating their response throughout the detection volume. For example, the XENON1T detector [?] is a TPC 1 m in diameter and in height,

Isotope	Half-life	Decay mode	Q-value (keV)
^{232}Th	1.41×10^{10} yr	α	4081
^{228}Ra	5.7 yr	β	46
^{228}Ac	6.15 hr	β	2124
^{228}Th	1.9 yr	α	5520
^{224}Ra	3.66 d	α	5989
^{220}Rn	55.6 s	α	6405
^{216}Po	0.145 s	α	6906
^{212}Pb	10.6 h	β	570
^{212}Bi	61 m	α (36%)	6207
		β (64%)	2252
^{212}Po	299 ns	α	8954
^{208}Tl	3.1 m	β	4999
^{208}Pb	Stable		

Table 5.1

The decay chain of primordial thorium, sometimes called the 4n series

much larger than e.g. the 70 mm mean free path of the 1.3 MeV γ from ^{60}Co . Thus, calibration of the entire fiducial volume with external sources is no longer feasible.

One solution is to directly mix a radioactive isotope into the liquid noble element. In liquid xenon, ^{83m}Kr has been proposed [?, ?, ?] and used [?] to achieve a low-energy γ -line calibration throughout the detector. Tritiated methane has been used as a low-energy beta source [?]. While this source has the advantage that all decays are in the low-energy range interesting to a dark matter search, it suffers from the disadvantage that the activity does not decay by itself but must be extracted from the liquid

target by a hot zirconium getter in a xenon recirculation loop [?]. This introduces an additional time constant that will get longer as the size of these detectors increases.

Here, we study a source containing ^{228}Th that emanates ^{220}Rn ($T_{1/2} = 56$ seconds), which in turn can be mixed into the liquid target. The ^{220}Rn decay chain is versatile, producing α -, β -, and γ -radiation that makes this source interesting for a wide range of applications: The source is the ideal calibration source for intrinsic ^{222}Rn backgrounds that are notoriously difficult to control in low-background experiments. (2) High-energy alphas [?, ?] and $^{212}\text{Bi}/^{212}\text{Po}$ decays [?] can be used to accurately understand intrinsic backgrounds. The relatively short half-life of ^{216}Po (145 ms) allows for the measurement of currents or liquid flows within the bulk of the detector volume. Using position reconstruction algorithms that yield the positions of the decays of ^{220}Rn and ^{216}Po together with the time difference between these two decays, allows for a measurement of the drift velocity of polonium ions [?]. Thus, currents within the bulk of the detector can be mapped to identify possible dead regions that do not participate in the recirculation of the active volume through purification systems. Additionally, the high-energy α lines can be used to probe regions in a detector with poor light or charge collection efficiency. Further, the ^{208}Tl decay produces a 2.6 MeV γ -line that can be used to calibrate the Q-value of the ^{136}Xe neutrinoless double-beta decay [?]. Finally, β -decays of the chain that go to the ground state can be used to calibrate the low-energy response of dark matter detectors. While the high Q-value of the ^{212}Bi β -decay (2.2 MeV) and short life-time of the daughter ^{212}Po (300 ns) render that decay unsuitable for this purpose, the β -decay of ^{212}Pb (12.3% branching ratio to ground state, Q-value 560 keV) is very suitable for this task, as shown in Figure 5.1.

A major advantage of our source is that the time scale of the ^{220}Rn decay chain is dominated by the relatively short half-life of ^{212}Pb ($T_{1/2} = 10.66$ hours). Thus, the introduced activity can completely decay away within a few days, making this source useful even for the largest anticipated liquid detectors [?, ?, ?]. As both ^{228}Th ($T_{1/2} = 1.9$ years) and ^{224}Ra ($T_{1/2} = 3.6$ days) have much longer half-lives, emanation of these

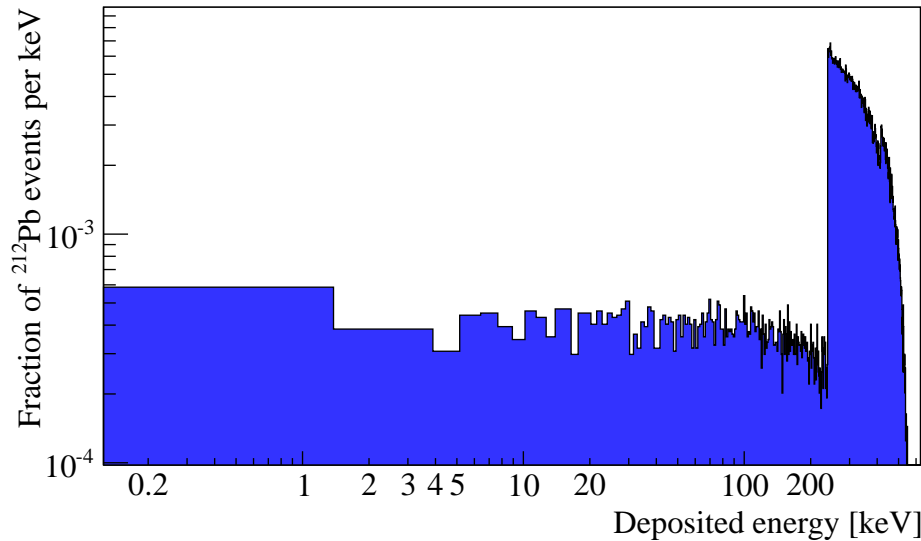


Figure 5.1. A simulation of the β -spectrum of ^{212}Pb . The feature at 240 keV is due to decay modes with an associated γ that adds to the energy observed in the decay.

isotopes from the source must be limited. Also, isotopic contaminations with ^{230}Th in the ^{228}Th source itself can lead to the emanation of ^{222}Rn ($T_{1/2} = 3.8$ days) which has to be avoided.

Here, we use a variety of methods to derive limits on the release of long-lived isotopes, and demonstrate that these sources are suitable for the calibration of even next-generation low-background experiments. Open ^{220}Rn sources were produced by electroplating thorium nitrate, $\text{Th}(\text{NO}_3)_4$, onto the center of a 30 mm diameter stainless steel disk in a bath of 1M nitric acid (HNO_3). A ring of width 2.5 mm around the edge of the disk was left for mounting purposes. The activity was 40 kBq as of March, 2015. Each source is held in a small stainless steel vessel to attach it to a noble gas recirculation system using 1/2" VCR piping, see figure 5.2.

5.2 γ -Measurements of Filter Deposition

The source was tested for the release of ^{224}Ra and ^{228}Th using a standard procedure. Nitrogen was flushed through the source vessel for 96 hours. A filter of

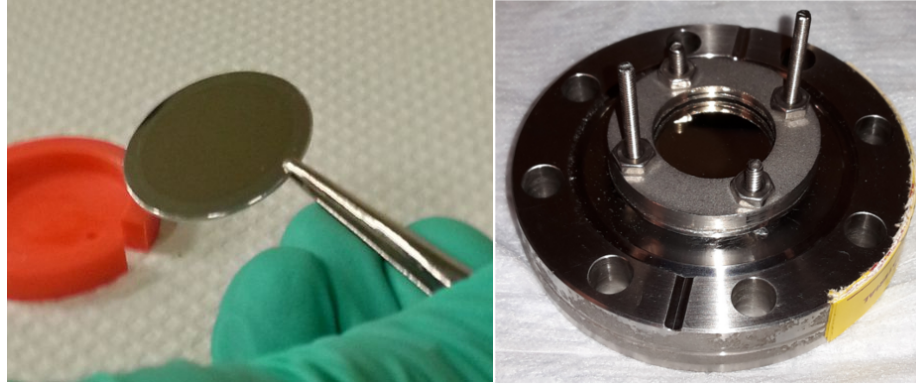


Figure 5.2. ^{228}Th is deposited onto a 30 mm stainless steel disc (left). It is held in a simple emanation vessel (right) for mounting on a noble gas system.

type ML050/0 was mounted inline 18 cm after the source, containing a filter paper on which any released radionuclides could be deposited. This filter paper was then tested for γ -activity with a high-purity germanium detector. A first measurement was made immediately after exposure, and a second measurement a week later, see Table 5.2.

Table 5.2
Measurements of radionuclide release from the ^{220}Rn source collected in filter paper.

Measurement	1	2
Time after exposure	Immediate	1 week
Livetime	375 s	11500 s
^{228}Th	< 35	< 1.97
^{224}Ra	< 6	< 0.61
Activity/Bq ^{212}Pb	87 ± 11	< 0.07
^{212}Bi	84 ± 34	< 0.68
^{208}Tl	28 ± 5	< 0.07

Both the exposure time and the time between measurements are significant compared to the half-life of ^{224}Ra . We account for both the decay during these intervals as well as the production of ^{224}Ra from the decay of ^{228}Th . The week between the two measurements is more than 15 half-lives of ^{212}Pb , hence any recorded activity of its daughters ^{212}Bi or ^{208}Tl in the second measurement would have been from the decay of ^{224}Ra , not any initial population of ^{212}Pb . We use the lowest measurement (here, ^{212}Pb) to constrain the release of ^{224}Ra from the source to < 0.43 atoms/s and that of ^{228}Th to or < 22 atoms/s. Scaling these values for the activity of the source yields a stray emanation of < 0.66 atoms/min/kBq ^{224}Ra and < 34 atoms/min/kBq ^{228}Th . We choose these units (atoms/min/kBq) to account for the decay of the sources over the time the various measurements were made, and to allow comparisons between the sources.

The obvious limitation of this measurement is that there may have been radium or thorium released by the source but not caught by the filter, in which case the given limits must be scaled by the efficiency of the filter. Additionally, any thorium or radium plated out on the pipes connecting the source vessel and the filter would not show up in this measurement.

A similar but more sensitive experiment was performed by pumping nitrogen at 1 standard liter per minute (slpm) for 9 days in a closed loop through the ^{220}Rn source vessel. The source was followed by a MILLEX-FG 50 filter at a distance of 8 cm, containing a $0.2\text{ }\mu\text{m}$ PTFE filter membrane. The exposure time brought any released ^{224}Ra nearly into equilibrium on the filter and gave potential ^{228}Th more time to deposit itself. After exposure, the filter membrane was tested for γ -activity with high-purity germanium detectors [?, ?]. A spectrum of these measurements is shown in figure 5.3. A simulation of the germanium crystal detector geometry performed in GEANT4 [?] indicated an efficiency of 6.5% at 240 keV.

A week after exposure most of the ^{212}Pb has decayed and measurements become sensitive to ^{224}Ra . A measurement with a livetime of 208 hours yielded a ^{224}Ra activity of (1.0 ± 0.3) Bq on the filter at the end of exposure. A second measurement was done

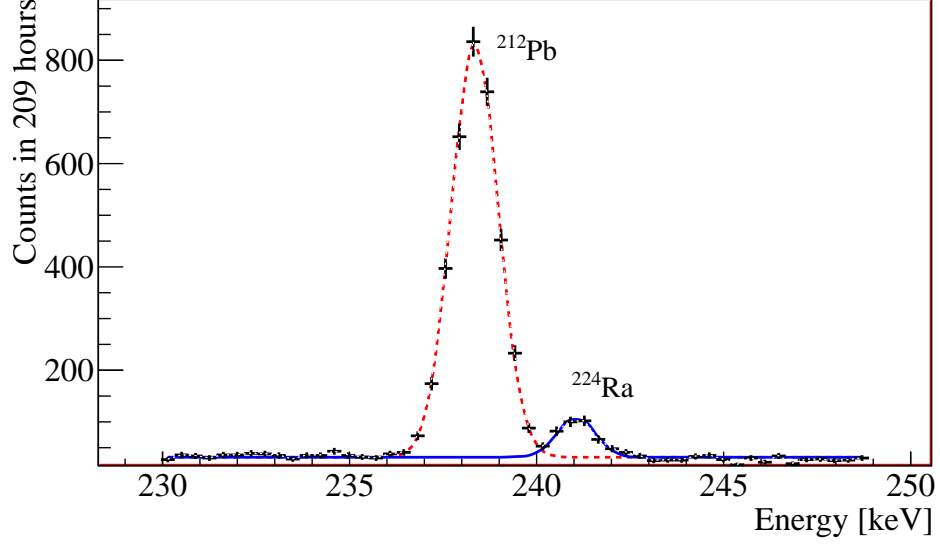


Figure 5.3. Gamma spectrum taken of the filter 7.2 days after exposure showing the ^{212}Pb line at 238.6 keV and the ^{224}Ra line at 241.0 keV. The dashed and solid lines are from a fit to the data.

forty-two days after exposure, at which point the ^{224}Ra deposited on the filter should have decayed to 3×10^{-4} of the initial population. Thus, any measured ^{224}Ra activity could be attributed to residual ^{228}Th . We calculate upper limits (90% CL) of 2.5 mBq for ^{228}Th and 2.4 mBq for ^{224}Ra on the filter. These activities convert to emanation rates of (1.9 ± 0.6) atoms/min/kBq ^{224}Ra and < 0.4 atoms/min/kBq ^{228}Th .

5.3 ^{222}Rn Emanation Measurement

Potential traces of ^{226}Ra or ^{230}Th in the ^{220}Rn source would lead to a non-negligible emanation of the long-lived radon isotope ^{222}Rn , which must be avoided. We applied ultra-low background proportional counters as described in [?] to measure directly the ^{222}Rn emanation rate of the source. For this purpose the source was connected to a 1 liter stainless steel buffer volume, separated by a valve. The setup was evacuated and the valve was opened such that ^{220}Rn and ^{222}Rn from the source could emanate into the buffer volume. After some days the valve was closed and the buffer volume was separated from the source. When all ^{220}Rn had decayed, the ^{222}Rn was extracted

from the buffer volume and filled to a proportional counter in which the alpha decays of ^{222}Rn and its daughters were counted.

We repeated the measurement three times with a small modification in the third measurement: Instead of emanating into vacuum, we filled 1.5 bar of helium in the buffer volume to check whether there is a difference between radon emanation into gas and into vacuum. It turned out that this is not the case as all three measurements are in good agreement and compatible with zero. The combined result is a ^{222}Rn emanation rate from the ^{220}Rn source of $< 55 \mu\text{Bq}$.

5.4 Si PIN Diode Measurements

A direct measurement of the ^{220}Rn source was performed with a custom-developed radon monitor. It consists of a 3-liter vacuum-tight stainless steel vessel containing a 2 cm square windowless Si PIN diode from Hamamatsu. A high voltage of 1.5 kV collects the charged ions resulting from the decays of ^{220}Rn onto the surface of the diode, where the ^{216}Po decay can be detected with an efficiency of about 35%. The radon detector was calibrated using a ^{226}Ra solution with a known activity of $(25 \pm 1) \text{ Bq}$ by bubbling nitrogen through the solution, thus obtaining a known activity of ^{222}Rn .

The ^{220}Rn source was placed directly inside the radon monitor, which was filled with air, and ^{220}Rn was allowed to reach equilibrium. Assuming the same collection efficiency of ^{222}Rn and ^{220}Rn , an emanation of $(1750 \pm 50) \text{ Bq}$ ^{220}Rn was determined. After 10 days, the ^{220}Rn source was removed from the radon monitor and the vessel evacuated, and all collected ions on the surface of the Si PIN diode were left to decay. Six days after the removal of the source, all ^{220}Rn activity would be due to emanated ^{224}Ra collected on the surface of the diode. The emanated ^{224}Ra activity was calculated to be $(2.1 \pm 0.7) \text{ Bq}$ and the ^{228}Th activity as $< 50 \mu\text{Bq}$ at the point when the source was removed, which corresponds to a ^{224}Ra emanation rate of $(3.9 \pm 1.3) \text{ atoms/min/kBq}$ and a ^{228}Th rate of $< 0.008 \text{ atoms/min/kBq}$.

To further determine levels of emanation, the source was placed directly facing a Hamamatsu windowless Si PIN diode that acts as an alpha spectrometer [?]. The source and diode were placed in a small vessel separated by only 8 mm. The vessel was then evacuated, and the source was left for five days to deposit material onto the surface of the diode. The source was then removed and the atoms deposited onto the diode were left to decay under vacuum. Figure 5.4 shows the total activity in the diode above 1 MeV decaying away after the removal of the source.

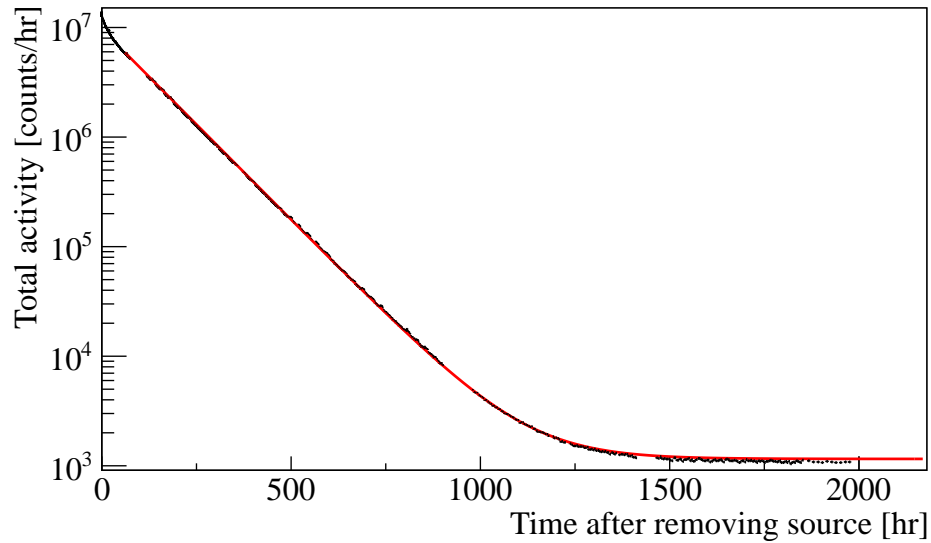


Figure 5.4. Total activity in the Si PIN diode above 1 MeV. The data points include statistical error bars, barely visible on this scale. The line is the fit of an exponential plus constant baseline.

An exponential decay plus a constant baseline is fit to this data, yielding a decay constant in agreement with the accepted half-life of ^{224}Ra , and a residual background of $(1128 \pm 3) \text{ hr}^{-1}$. Extrapolating the curve backwards and scaling for the fraction of total activity that is ^{224}Ra , we can calculate the emanation rate of ^{224}Ra onto the surface of the diode to be $(924.0 \pm 0.3) \text{ s}^{-1}$. Two months after removing the source, the initial population of ^{224}Ra will have decayed away, so the background value inferred from the fit is due to a combination of intrinsic backgrounds (here, measured to be negligible) and released ^{228}Th . By measuring the activity in the relevant portion of

the spectrum, we find a ^{228}Th activity of $(0.097 \pm 0.003) \text{ Bq}$, or $(8.4 \pm 0.3) \times 10^6$ atoms. Given the exposure time, this corresponds to a ^{228}Th emanation rate of $(18.3 \pm 0.6) \text{ s}^{-1}$ onto the surface of the diode. Simulation with GEANT4 yields a geometric efficiency for deposition of 0.13, which allows us to scale the emanation rates of the source to $(4.5 \pm 0.2) \text{ atoms/s/kBq } ^{228}\text{Th}$ and $(282.1 \pm 0.1) \text{ atoms/s/kBq } ^{224}\text{Ra}$.

5.5 γ -Spectroscopy of Pipe Contamination

A test of radium plate-out was performed by flushing argon from a high-pressure tank through a pressure regulator, the source vessel, and then a copper pipe of 6 mm diameter and 50 cm length. The argon flow averaged 6 slpm though with sizeable fluctuations. After 41 hours of flushing, the copper pipe was cold-welded shut at both ends to seal in any materials deposited on the inner surface, and swiftly transported for measurement using our low-background germanium counters. Several measurements were done over the course of about two months to determine the γ -activity of the copper pipe. The results of the measurements are given in Table 5.3.

Table 5.3
Results of the measured γ -activity in the cold-welded copper pipe after flushing argon through source and pipe.

Measurement	1	2	3
Time after exposure	10 hours	7 days	68 days
Livetime	76733 s	897820 s	357802 s
Activity/Bq ^{224}Ra	N/A	0.25 ± 0.03	< 0.088
Activity/Bq ^{212}Pb	13.8 ± 0.1	0.215 ± 0.005	< 0.088

The interpretation of these data is done in a very similar way to that presented in the previous section. The first measurement started approximately 1 half-life of ^{212}Pb after exposure, so any amount deposited on the pipe would still be observ-

able. By the time the second measurement was started, a week had passed (>15 half-lives), so any initial ^{212}Pb would have decayed to a negligible amount, making the measurement sensitive to potential ^{212}Pb from the decay of ^{224}Ra . The interval between exposure and the third measurement is many half-lives of ^{224}Ra , making the measurement sensitive to potential contamination from the parent ^{228}Th in the copper pipe.

Table 5.4
Calculated values and limits on ^{224}Ra and ^{228}Th release from deposition in the copper pipe after argon flushing.

Isotope	Activity after exposure	Emanation rate
^{212}Pb	$(26.0 \pm 0.2) \text{ Bq}$	N/A
^{224}Ra	$(0.95 \pm 0.11) \text{ Bq}$	$(1.53 \pm 0.04) \text{ atoms/min/kBq}$
^{228}Th	$< 0.093 \text{ Bq}$	$< 47 \text{ atoms/min/kBq}$

Indeed trace amounts of ^{224}Ra appear to have come off the source in this experiment. While the overall activity is very small, it motivates the use of an additional filter just after the source vessel for the calibration of low background detectors.

5.6 Measurements of Filter Efficacy

In order to assess the performance of various filters in limiting the release of ^{224}Ra from the ^{220}Rn source, the source vessel was connected to a xenon gas system. Xenon gas was recirculated through various configurations involving the ^{220}Rn source vessel, filters, and a Si PIN diode as an α -spectrometer [?]. The source was exposed to the xenon gas stream for a few days, then bypassed, and the decaying activity monitored to measure any released radium. Two filter types were tested for their ability to remove radium from the gas stream. The first filter was a Swagelok F-series 0.5-micron sintered filter, the second was a Swagelok SCF-series ceramic filter.

The source vessel was connected directly to the sintered filter and then to the Si PIN diode with about 1 m of 1/4" stainless steel pipe. For the ceramic filter, the extra piping was reduced to 8 cm. Xenon gas at 1 barg was recirculated through the gas system at 5 slpm for the sintered filter and 10 slpm for the ceramic filter. After exposure with the sintered filter in line, the source and filter were bypassed and recirculation continued through the detector vessel for several weeks. After exposure with the ceramic filter, recirculation was stopped and the activity deposited in the detector vessel left to decay. Figure 5.5 shows the activity of coincident ^{212}Bi - ^{212}Po (BiPo) activity in the Si PIN diode for the measurement of the ceramic filter from when the source was opened to three days after the source was closed, when the detector vessel was evacuated.

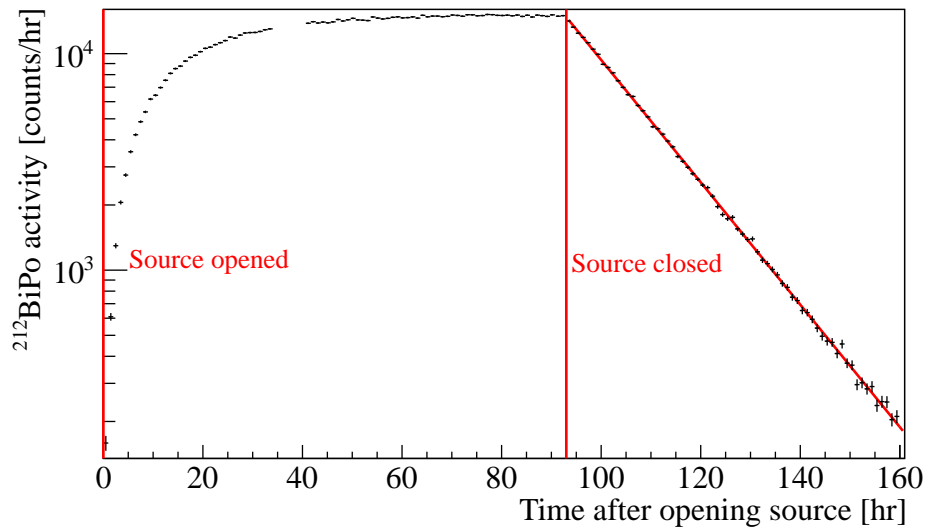


Figure 5.5. Activity of $^{212}\text{BiPo}$ in the Si PIN diode during and after flushing xenon through the ceramic filter. An exponential was fitted to the decaying part, yielding a half-life of (10.64 ± 0.05) h in excellent agreement with the ^{212}Pb half-life of (10.64 ± 0.01) h [?].

The activity in the Si PIN diode was monitored as the released ^{212}Pb decayed to background levels. A summary of the results are given in Table 5.5. About 14 half-lives after closing the source the ^{212}Pb has almost completely decayed to background levels, at which point any measurement would be sensitive to the release of ^{224}Ra .

The background rate of $^{212}\text{BiPo}$ events was found prior to these measurements to be $(42 \pm 7) \mu\text{Bq}$. Figure 5.6 shows the decay for the measurement of the sintered filter, along with a fitted exponential and constant.

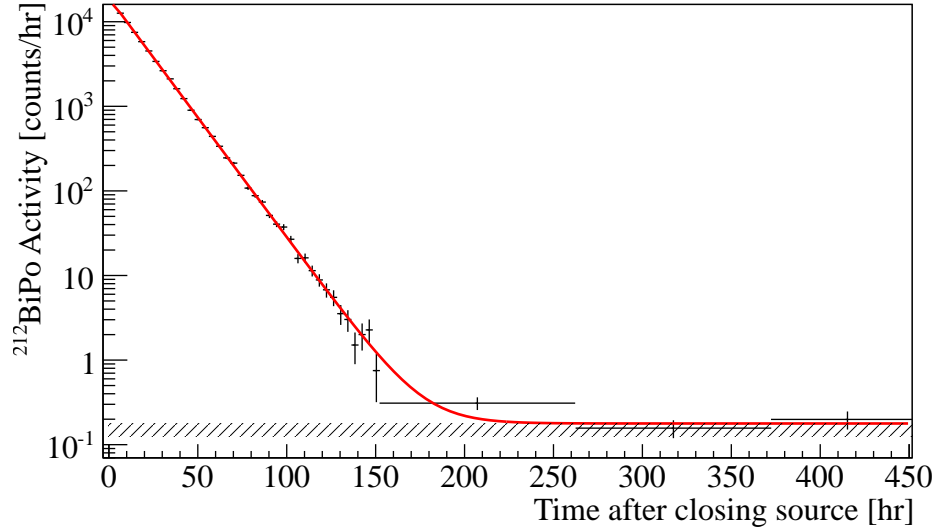


Figure 5.6. Decay to background of $^{212}\text{BiPo}$ in the Si PIN diode for the measurement of the sintered filter. An exponential and a constant are fitted to the data. The band is the previously measured background of the detector.

Table 5.5
Measurement results for the 0.5 micron sintered and ceramic filters

Filter	Exposure	Fitted half-life	Fitted background
Sintered	39 hr	$(10.64 \pm 0.11) \text{ hr}$	$(49 \pm 8) \mu\text{Bq}$
Ceramic	93 hr	$(10.51 \pm 0.60) \text{ hr}$	$(46 \pm 8) \mu\text{Bq}$

Both background values show some increase over the rate measured before this experiment, but in neither case is the increase statistically significant (1σ for the sintered filter, 0.43σ for the ceramic filter). However, we can still (conservatively) attribute these small increases to some released ^{224}Ra , in which case we can limit the release of ^{224}Ra to $< 0.65 \text{ atoms/day/kBq}$ for the sintered filter and $< 0.21 \text{ atoms/day/kBq}$

for the ceramic filter. Thus we see that both filters are highly effective at preventing the release of ^{224}Ra from the source.

A more direct measurement of filter efficiency was performed by placing two identical 90 micron sintered filters in series in the gas system immediately after the source vessel. After recirculating xenon gas at 6.5 SLPM through the source and filters for 100 hours, the two filters were then placed on top of the Si PIN diode to measure any α -activity coming off of them that could be attributed to ^{224}Ra . A total of 4 days of data were taken. The spectra of the two filters is shown in Figure 5.7. While the first filter showed an activity of (55.4 ± 2.1) mBq of ^{224}Ra , the second filter that was placed immediately downstream of the first only showed an activity of (1.63 ± 0.18) mBq of ^{224}Ra . Both numbers are corrected for the activity at the time of source closing. Hence, their ratio directly gives the filter efficiency. This value is independent of systematic uncertainties such as the collection efficiency of the Si PIN diode, geometrical effects, etc. We thus find these 90 micron sintered filters to retain $(97.1 \pm 0.3)\%$ of ^{224}Ra flushing through them.

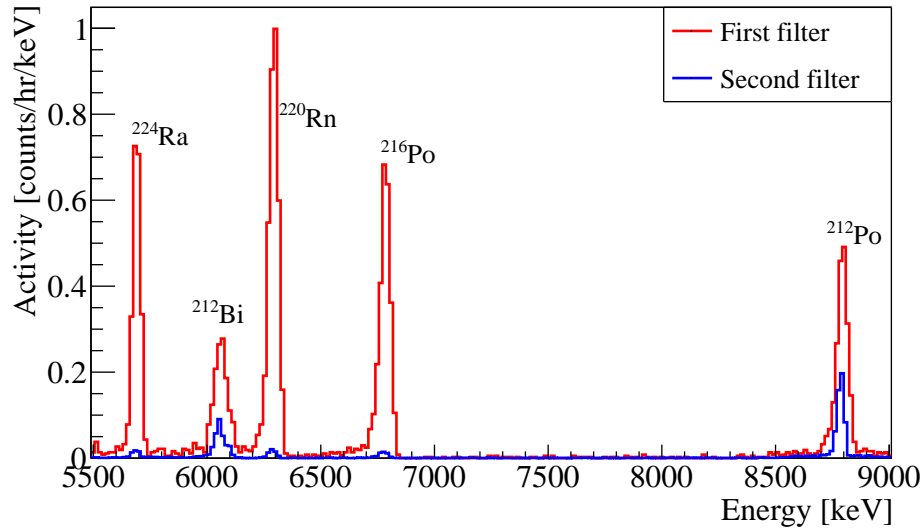


Figure 5.7. Energy spectrum taken with the Si PIN diode from two sintered filters that were placed in series directly after the source in a xenon gas recirculation system.

5.7 Mixing in a Liquid Xenon Detector

A liquid/gas xenon TPC was used to test the injection of ^{220}Rn into a liquid xenon detector. The detector was designed with a long drift length of 17 cm and a diameter of 80 mm. Each end of the drift chamber is monitored by 7 Hamamatsu R8720 photomultiplier tubes (PMTs). The walls of the TPC are constructed of a single cylinder of PTFE, for use as a UV light reflector, with field shaping electrodes embedded inside the PTFE walls. The drift and charge amplification fields are applied with transparent meshes at the ends of the TPC to allow for high optical collection. For the measurements presented here, the detector was operated in a single-phase mode, with the full detector flooded with liquid xenon. This setup is sufficient to demonstrate that ^{220}Rn can be flushed into the detector before decaying so that the subsequent ^{212}Pb beta decays can be used as an internal calibrator. The detector was filled with about 3 kg of liquid xenon, which was continuously recirculated through a high-temperature zirconium getter to remove electronegative impurities. The recirculation is done in the gas phase using 1/2" VCR piping with a heat exchanger in the xenon loop [?], constituting a setup very similar to that of the XENON1T experiment [?]. The ^{220}Rn source vessel was connected to the gas recirculation system such that the gas could be flushed past the source or bypass it. Figure 5.8 shows a schematic of the detector, purification loop, and ^{220}Rn source. About 5 m of piping connected the ^{220}Rn source to the TPC.

To prove that the ^{220}Rn could be mixed into the detector, the source was opened for 22.8 hours, injecting the doped gas. By monitoring the trigger rate of the detector in single phase operation, it was possible to observe the arrival of the dopants into the liquid xenon target. Data were acquired for 2.9 days surrounding this opening to determine the background before opening, and to monitor the decay of the injected ^{212}Pb after the source was closed. The resulting trigger rate evolution is shown in Figure 5.9. The background trigger rate of 200 Hz quickly rose to a saturated rate of around 550 Hz after the source was opened, showing that the activity of the source

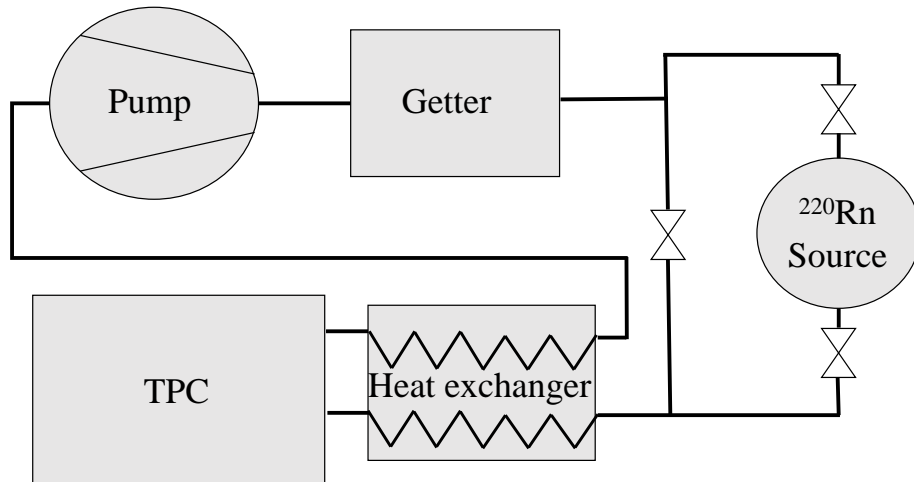


Figure 5.8. Schematic of the recirculation loop for the liquid xenon detector measurement. The liquid is evaporated in the heat exchanger and is pumped through the purifier, where it can then be flushed past the ^{220}Rn source or injected directly back to the detector.

was entering the liquid xenon target. After the source was closed, the trigger rate quickly dropped to 450 Hz, after which it decayed toward the background rate.

The data acquisition system was not optimized for measuring high rates in a single phase operation, resulting in a large rate-dependent dead time. This impedes our determination of the actual activity in the target volume, as well as our ability to fit the observed decay to a single exponential. However, this measurement is clearly sufficient to demonstrate three major features of this source: first, ^{220}Rn emanates from the source and can be mixed into a liquid xenon detector. Second, a low activity source is capable of introducing enough activity to be measured even above a high background rate. Third, the decay after the source is closed demonstrates the presence of ^{212}Pb in the liquid target, a requirement to use this source for calibration of the low-energy region in a dark matter search.

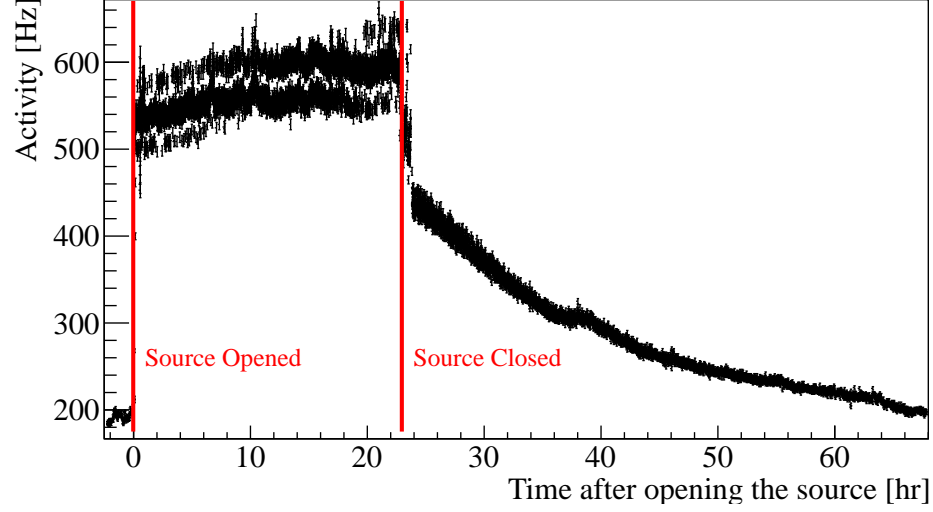


Figure 5.9. Trigger rate in the liquid xenon detector before, during, and after source exposure. The spike in the rate after opening the source clearly shows the introduction of activity into the target volume, and the decay after it the source was closed indicates the presence of ^{212}Pb .

Table 5.6

Summary of all measurements of emanation rates, given in units of atoms/min/kBq.

Measurement	^{228}Th	^{224}Ra
γ measurements of filters, Section 5.2	< 34	< 0.66
	< 0.4	1.9 ± 0.6
Pipe contamination, Section 5.5	< 47	1.53 ± 0.04
Radon monitor, Section 5.4	< 0.008	3.9 ± 1.3
Si PIN diode, Section 5.4	270 ± 12	16926 ± 6
Sintered filter, Section 5.6	N/A	$< 4.5 \times 10^{-4}$
Ceramic filter, Section 5.6	N/A	$< 1.5 \times 10^{-4}$

5.8 Interpretation

Table 5.6 summarizes the various measurements. The two γ measurements of filter deposition and the measurement of pipe contamination are methodologically

very similar, yet the results are strikingly different. Additionally, the measurement using the Si PIN diode are orders of magnitude different. The apparent inconsistency between the γ measurements and pipe contamination can be attributed to deposition of ^{224}Ra in the 1/2" piping: in the first two measurements, 18 cm and 8 cm of piping were present respectively in between the source vessel and filter, while the copper pipe was less than 1 cm from the source (leaving just enough space to cold-weld the copper). In the second γ measurement, the flow through the source vessel and the filter was laminar, whereas the flow was turbulent for the pipe contamination measurement. Due to its extremely high reactivity, radium will bond readily to pipe walls. This is facilitated by turbulent flow, while in laminar flow, the slow process of radial diffusion will impede the plate-out of ^{224}Ra . As the second γ measurement and the pipe contamination measurement are consistent, we attribute the discrepancy of the first γ measurement to the different conditions of the gas flow.

For the measurements of filter efficiency, the limits presented for the ceramic and 0.5 micron sintered filters are very satisfactory, while in the two-filter measurement, the 90 micron sintered filters are only 97% efficient. However, at the time of this measurement, the source had an activity of around 60 kBq. Hence, the activity seen in the first filter (55.4 ± 2.1 mBq) shows a drastic reduction in the activity after only a few centimeters of piping. From this, we can conclude that even though the source gives off very large amounts of ^{224}Ra and ^{228}Th (as shown by the Si PIN diode measurement), only a vanishing percentage makes it out of the source vessel. With these sources being used in a fluid stream, one may thus expect the vast majority of ^{224}Ra and ^{228}Th to plate out in any connecting piping.

5.9 Conclusions

We have presented a versatile ^{220}Rn source for the internal calibration of low-background detectors and demonstrated its suitability. Stray emanation was found to be < 0.008 atoms/min/kBq for ^{228}Th and (1.53 ± 0.04) atoms/min/kBq for ^{224}Ra ,

which can be reduced to $< 10^{-3}$ atoms/min/kBq through the use of an additional filter. We have demonstrated that the ^{220}Rn activity can be mixed under realistic conditions in a liquid noble gas detector. The source provides the means by which to calibrate the electronic recoil band in liquid noble element dark matter detectors at low energies, characterize the important radon backgrounds, map fluid dynamics in the liquid target and possibly calibrate the Q-value of ^{136}Xe double-beta decay.

APPENDICES

VITA

VITA

[Put a brief autobiographical sketch here.]